

## ARTICLE OPEN



# Charge order in the kagome lattice Holstein model: a hybrid Monte Carlo study

Owen Bradley<sup>1</sup>✉, Benjamin Cohen-Stead<sup>1,2,3</sup>, Steven Johnston<sup>2,3</sup>, Kipton Barros<sup>4</sup> and Richard T. Scalettar<sup>1</sup>

The Holstein model is a paradigmatic description of the electron-phonon interaction, in which electrons couple to local dispersionless phonon modes, independent of momentum. The model has been shown to host a variety of ordered ground states such as charge density wave (CDW) order and superconductivity on several geometries, including the square, honeycomb, and Lieb lattices. In this work, we study CDW formation in the Holstein model on the kagome lattice, using a recently developed hybrid Monte Carlo simulation method. We present evidence for  $\sqrt{3} \times \sqrt{3}$  CDW order at an average electron filling of  $\langle n \rangle = 2/3$  per site, with an ordering wavevector at the  $K$ -points of the Brillouin zone. We estimate a phase transition occurring at  $T_c \approx t/18$ , where  $t$  is the nearest-neighbor hopping parameter. Our simulations find no signature of CDW order at other electron fillings or ordering momenta for temperatures  $T \geq t/20$ .

*npj Quantum Materials* (2023)8:21 | <https://doi.org/10.1038/s41535-023-00553-y>

## INTRODUCTION

The interaction between electrons in a solid and the vibrations of its nuclei (phonons) can induce a variety of ordered phases<sup>1–6</sup>. This electron-phonon coupling modifies the effective mass of itinerant electrons, and the resulting dressed quasiparticles (polarons) can pair and condense into a superconducting (SC) phase or form a periodic modulation of electron density, i.e., CDW order. At low temperatures, these various phases can compete or potentially coexist. Over the past several decades, studies of model Hamiltonians describing electron-phonon coupling have attempted to capture the interplay between their emergent ordered phases. In particular, the Holstein model<sup>7</sup> has been subject to much numerical and analytical study because it incorporates a simplified electron-phonon interaction into a straightforward tight-binding Hamiltonian, yet exhibits a variety of competing ordered ground states.

A key feature of the Holstein model is an on-site momentum-independent electron-phonon coupling, which leads to an effective electron-electron attraction. Phonons are modeled as quantum harmonic oscillators of fixed frequency  $\omega_0$  situated on each site of a lattice, with their motion independent of their neighbors. At low temperatures and at particular electron filling fractions, numerical studies have revealed the emergence of CDW order on square<sup>8–22</sup>, triangular<sup>23</sup>, cubic<sup>24</sup>, and honeycomb lattices<sup>25,26</sup>, with the transition temperature being sensitive to lattice geometry and dimensionality. A recent study of the Lieb lattice has also established the existence of CDW order in the Holstein model in a flat band system<sup>27</sup>.

In recent years, kagome lattices have attracted attention as a host of exotic phases owing to their high degree of geometrical frustration, and the presence of a flat band. The spin-1/2 kagome lattice Heisenberg antiferromagnet (KHAF) with nearest-neighbor interactions lacks any magnetic ordering, but the exact nature of the ground state has been subject to much debate, with several candidates such as the Dirac spin-liquid,  $Z_2$  spin-liquid, and valence bond crystal proposed<sup>28–31</sup>. A recent study of the KHAF in

the presence of spin-lattice coupling has shown that introducing Einstein phonons on each site can induce a magnetically ordered phase<sup>32</sup>. For example, a  $\sqrt{3} \times \sqrt{3}$  ordered phase with a 1/3-magnetization plateau emerges in weak magnetic field, breaking a  $Z_3$  symmetry, with the transition belonging to the 3-state Potts model universality class. The ordering wavevector for this phase lies at the  $K$ -points, i.e., corners, of the hexagonally-shaped Brillouin zone.

The ground state properties of the half-filled kagome lattice Hubbard model are also debated. Dynamical mean field theory (DMFT) and determinant quantum Monte Carlo (DQMC) studies have identified a metal-insulator transition (MIT) in the range  $U_c/t \sim 7–9$ <sup>33–35</sup>, while variational cluster approximation (VCA) calculations estimate  $U_c/t \sim 4–5$ <sup>36</sup>. Recent density-matrix renormalization group (DMRG) calculations find a MIT at  $U_c/t \sim 5.4$ , along with strong spin-density wave fluctuations in the translational symmetry breaking insulating phase, signaled by an enhancement in the spin structure factor at the  $K$ -points of the Brillouin zone<sup>37</sup>. CDW formation on the kagome lattice has also been observed in the extended Hubbard model. At an average electron density per site of  $\langle n \rangle = 2/3$  or  $4/3$ , or at the van Hove filling  $\langle n \rangle = 5/6$ , several types of order have been observed<sup>38–41</sup>, including CDW, spin-density wave, and bond ordered wave states. In particular, at large  $V/U$  (where  $V$  is the nearest-neighbor repulsion), a CDW phase with a  $\sqrt{3} \times \sqrt{3}$  supercell has been proposed for  $\langle n \rangle = 2/3$  and  $5/6$ , which has been termed CDW-III in previous studies<sup>40,41</sup>. In the attractive Hubbard model, recent results<sup>42</sup> indicate short-ranged charge correlations at  $\langle n \rangle = 2/3$  satisfying the triangle rule.

Recent experiments on kagome metals such as  $AV_3Sb_5$  ( $A = K, Rb, Cs$ ) also motivate an understanding of CDW formation on this geometry<sup>43–55</sup>. In these systems, charge ordering has been observed at the  $M$ -points, corresponding to lattice distortions that form a star-of-David or inverse star-of-David CDW pattern. This ordering wavevector coincides with saddle points in the band structure and van Hove singularities where electronic correlations are enhanced. Theoretical studies of these materials<sup>56–64</sup>,

<sup>1</sup>Department of Physics, University of California, Davis, CA 95616, USA. <sup>2</sup>Department of Physics and Astronomy, The University of Tennessee, Knoxville, TN 37996, USA. <sup>3</sup>Institute for Advanced Materials and Manufacturing, The University of Tennessee, Knoxville, TN 37996, USA. <sup>4</sup>Theoretical Division and CNLS, Los Alamos National Laboratory, Los Alamos, NM 87545, USA. ✉email: [opbradley@ucdavis.edu](mailto:opbradley@ucdavis.edu)

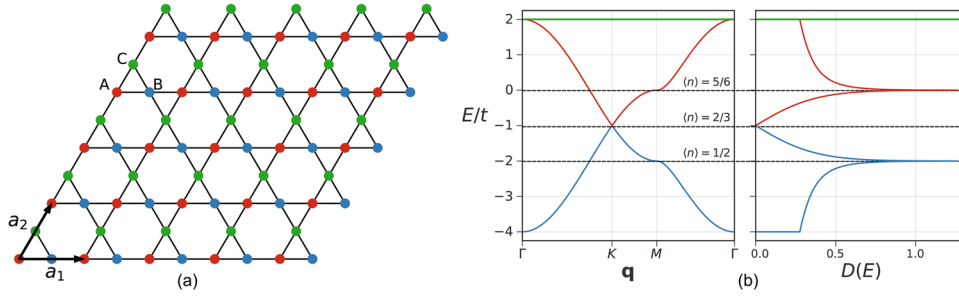


**Fig. 1 Kagome lattice and band structure.** **a** Geometry of the kagome lattice for  $L = 6$ , with lattice vectors  $\mathbf{a}_1 = (1, 0)$  and  $\mathbf{a}_2 = (\frac{1}{2}, \frac{\sqrt{3}}{2})$ . Colors denote the three triangular sublattices. **b** Left: The tight-binding electronic band structure for the kagome lattice showing the three distinct bands. Dashed lines indicate the Fermi energy at specific electron densities. Right: The non-interacting density of states  $D(E)$  for the kagome lattice. A delta function at  $E = 2t$  is due to the flat band.

including first-principles density functional theory and mean field calculations, have corroborated these findings, where CDW ordering at the  $M$ -points has been observed near the van Hove filling.

Finally, kagome lattices have also been achieved in ultracold atom experiments<sup>65</sup> where they have been used to examine Bose-Einstein condensation of <sup>87</sup>Rb<sup>66</sup>, and Rydberg atoms with large entanglement entropy and topological order<sup>67</sup>.

Although the Holstein coupling provides a paradigmatic model of the electron-phonon interaction, the properties of the Holstein model on the kagome lattice are not yet understood, and the possible existence of CDW order remains hitherto unexplored. In this work, we study the kagome lattice Holstein model using a scalable algorithm based upon hybrid Monte Carlo (HMC) sampling<sup>68</sup>, and measure the charge correlations as a function of temperature, electron density, phonon frequency, and electron-phonon coupling. We present evidence for CDW order appearing at an average electron density per site of  $\langle n \rangle = 2/3$ , with an ordering wavevector at the  $K$ -points of the Brillouin zone, yielding a  $\sqrt{3} \times \sqrt{3}$  supercell. Away from this filling, we find no signatures of CDW order at any ordering momenta for temperatures  $T \geq t/20$ .

## RESULTS

### Kagome lattice Holstein model

The Holstein model describes electrons coupled to local dispersionless phonon modes in a lattice through an on-site electron-phonon interaction<sup>7</sup>. Its Hamiltonian is

$$\hat{H} = -t \sum_{\langle i,j \rangle, \sigma} (\hat{c}_{i\sigma}^\dagger \hat{c}_{j\sigma} + h.c.) - \mu \sum_{i\sigma} (\hat{n}_{i\sigma} - \frac{1}{2}) + \frac{1}{2} \sum_i \hat{P}_i^2 + \frac{\omega_0^2}{2} \sum_i \hat{X}_i^2 + \lambda \sum_{i\sigma} \hat{n}_{i\sigma} \hat{X}_i, \quad (1)$$

where  $\hat{c}_{i\sigma}^\dagger$  ( $\hat{c}_{i\sigma}$ ) are creation (destruction) operators for an electron at site  $i$  with spin  $\sigma = \{\uparrow, \downarrow\}$ ,  $\hat{n}_{i\sigma} = \hat{c}_{i\sigma}^\dagger \hat{c}_{i\sigma}$  is the electron number operator, and  $\mu$  is the chemical potential, which controls the overall filling fraction. The first term describes itinerant electrons hopping between nearest-neighbor sites of the lattice, with a fixed hopping parameter  $t=1$  setting the energy scale. In the non-interacting limit, the electronic bandwidth is  $W=6$  for the kagome lattice. On each site  $i$  are local oscillators of fixed frequency  $\omega_0$ , with  $\hat{X}_i$  and  $\hat{P}_i$  the corresponding phonon position and momentum operators, respectively, with the phonon mass normalized to  $M=1$ . The local electron density  $\hat{n}_{i\sigma}$  is coupled to the displacement  $\hat{X}_i$  through an on-site electron-phonon interaction  $\lambda$ , which we report here in terms of a dimensionless parameter  $\lambda_D = \lambda^2 / \omega_0^2 W$ .

The kagome lattice vectors  $\mathbf{a}_1 = (1, 0)$  and  $\mathbf{a}_2 = (\frac{1}{2}, \frac{\sqrt{3}}{2})$  are shown in Fig. 1a, with corresponding reciprocal lattice vectors  $\mathbf{b}_1 = (2\pi, -\frac{2\pi}{\sqrt{3}})$  and  $\mathbf{b}_2 = (0, \frac{4\pi}{\sqrt{3}})$ , where we have set the lattice

constant  $a = 1$ . There are three sites per unit cell with basis vectors  $\mathbf{u}_A = (0, 0)$ ,  $\mathbf{u}_B = (\frac{1}{2}, 0)$ , and  $\mathbf{u}_C = (\frac{1}{4}, \frac{\sqrt{3}}{4})$ , forming a network of corner sharing triangles with three sublattices, as shown in Fig. 1a. Each site  $i$  may instead be indexed by unit cell and the sublattice  $\{A, B, C\}$ , such that e.g.,  $n_{i,\alpha}$  denotes the electron density at the site belonging to sublattice  $\alpha$  within the unit cell at position  $\mathbf{i}$ . In this work, we study finite-size lattices with periodic boundary conditions, with linear dimension  $L$  (up to  $L = 15$ ),  $N = L^2$  unit cells, and  $N_s = 3N$  total sites. Note that discrete momentum values are given by  $\mathbf{k} = \frac{m_1}{L} \mathbf{b}_1 + \frac{m_2}{L} \mathbf{b}_2$  where  $m_i$  is an integer and  $0 \leq m_i < L$ .

There are multiple ways to break the sublattice symmetry of the kagome lattice. It is, therefore, important to construct an order parameter that will detect charge ordering independent of the charge distribution within the unit cell. For example, at a filling fraction of  $1/3$ , electrons may localize by doubly occupying only one site per unit cell, breaking a  $Z_3$  symmetry. We, therefore, define an order parameter  $\rho_{\text{cdw}}$  that with perfect CDW order takes on one of three values  $e^{i2\pi(\frac{s}{3})}$ , where  $s = \{0, 1, 2\}$  corresponds to which way this symmetry is broken. The order parameter  $\rho_{\text{cdw}}$  should also be zero in the completely disordered state, where for any unit cell  $\mathbf{i}$  we have  $\langle \hat{n}_{i,A} \rangle = \langle \hat{n}_{i,B} \rangle = \langle \hat{n}_{i,C} \rangle$ . Hence we define

$$\rho_{\text{cdw}} = \frac{n_c}{2N} \sum_{\mathbf{i}} e^{-i(\mathbf{q} \cdot \mathbf{i})} \left( \langle \hat{n}_{i,A} \rangle + e^{i\frac{2\pi}{3}} \langle \hat{n}_{i,B} \rangle + e^{i\frac{4\pi}{3}} \langle \hat{n}_{i,C} \rangle \right) \quad (2)$$

where  $\mathbf{i}$  is a unit cell index,  $N$  is the total number of unit cells,  $\mathbf{q}$  is the ordering wavevector, and  $n_c$  is a normalization constant included to fix  $|\rho_{\text{cdw}}| = 1$  in the case of perfect CDW order. A structure factor that scales with system size can then be defined as  $S_{\text{cdw}}(\mathbf{q}) \propto N(|\hat{\rho}_{\text{cdw}}|^2)$ , where again a proportionality constant can be included to fix  $S_{\text{cdw}}(\mathbf{q}) = N$  for the case of perfect CDW order.

For any pair of sites in the kagome lattice, we denote their density-density correlation in position space by

$$c_{\alpha,\nu}(\mathbf{r}) = \frac{1}{N} \sum_{\mathbf{i}} \langle \hat{n}_{\mathbf{i}+\mathbf{r},\alpha} \hat{n}_{\mathbf{i},\nu} \rangle, \quad (3)$$

where  $\alpha$  and  $\nu$  label the sublattice  $\{A, B, C\}$  of the two sites, and  $\mathbf{r}$  is the displacement vector between their unit cells. The Fourier transform of  $c_{\alpha,\nu}(\mathbf{r})$  gives a generic charge structure factor

$$S_{\alpha,\nu}(\mathbf{q}) = \sum_{\mathbf{r}} e^{i\mathbf{q} \cdot \mathbf{r}} c_{\alpha,\nu}(\mathbf{r}), \quad (4)$$

which provides information about the nature of an emergent CDW phase, where  $\mathbf{q}$  is a discrete momentum value within the first Brillouin zone. For an ideal CDW pattern with ordering wavevector  $\mathbf{q}$ ,  $S_{\alpha,\alpha}(\mathbf{q})$  will reach a maximal value proportional to the number of sites, while for  $\alpha \neq \nu$  the structure factor will vanish.

In the following section, we show evidence of CDW ordering on the kagome lattice where electrons localize on only one site per unit cell but alternates cyclically between the  $\{A, B, C\}$  sublattices from one unit cell to the next. To study the onset of this phase, we

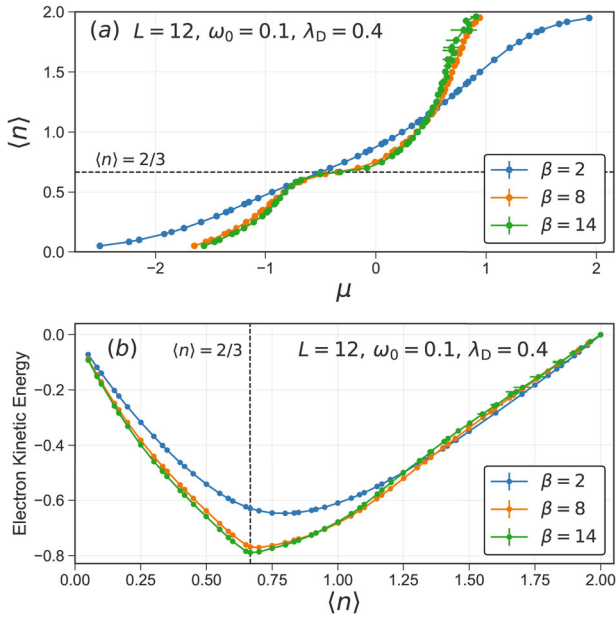


**Fig. 2 Electron density and kinetic energy.** **a** Average electron density per site  $\langle n \rangle$  as a function of the tuned chemical potential  $\mu$ , for an  $L = 12$  lattice with  $\omega_0 = 0.1$  and  $\lambda_D = 0.4$  fixed. Results are shown for  $\beta = 2, 8$ , and  $14$ , with a dashed line indicating the filling  $\langle n \rangle = 2/3$ . **b** Electron kinetic energy as a function of the electron density  $\langle n \rangle$ , for the same set of parameters. Error bars correspond to the standard deviation of the measured mean.

set  $n_c = 1$  in Eq. (2) and define a charge structure factor

$$\begin{aligned} S_{\text{cdw}}(\mathbf{q}) &= 3N \langle |\hat{\rho}_{\text{cdw}}|^2 \rangle \\ &= \frac{3}{4} \sum_{\alpha} \left( S_{\alpha,\alpha}(\mathbf{q}) - \frac{1}{2} \sum_{\nu \neq \alpha} S_{\alpha,\nu}(\mathbf{q}) \right). \end{aligned} \quad (5)$$

Additional details are given in Supplementary Discussion. Note that we employ a  $\mu$ -tuning algorithm<sup>69</sup> to determine the chemical potential for any desired target density.

### Measurements of charge order

For the kagome lattice, the non-interacting tight-binding electronic structure with  $t > 0$  has three separate bands, including one flat band at the highest energy ( $E = 2t$ ). The lower bands touch at two inequivalent Dirac points in the Brillouin zone, which we denote  $K = (\frac{2\pi}{3}, \frac{2\pi}{\sqrt{3}})$  and  $K' = (\frac{4\pi}{3}, 0)$ . The lower band is completely occupied at an average electron density per site of  $\langle n \rangle = 2/3$  (i.e., an overall filling fraction of  $f = 1/3$ ), while the upper band is fully occupied at  $\langle n \rangle = 4/3$  ( $f = 2/3$ ). There are also saddle points in the band structure at the point  $M = (\pi, \frac{\pi}{\sqrt{3}})$ , which produce singularities in the density of states and sit at the Fermi level for average electron densities of  $\langle n \rangle = 1/2$  ( $f = 1/4$ ) and  $\langle n \rangle = 5/6$  ( $f = 5/12$ ). Fig. 1b plots the non-interacting band structure and density of states for the kagome lattice, illustrating these features.

To begin, we study the variation of local quantities as a function of electron density, at fixed  $\omega_0$  and  $\lambda_D$ . We set  $\omega_0/t = 0.1$  to facilitate CDW ordering in the Holstein model, as bipolarons should localize more readily in the limit  $\omega_0/t \rightarrow 0$  due to reduced quantum fluctuations. We also fix a moderate value of the electron-phonon coupling  $\lambda_D = 0.4$ . We will discuss the rationale for this choice of parameters shortly.

In Fig. 2a, we show the average electron density per site  $\langle n \rangle$  as a function of chemical potential  $\mu$  for an  $L = 12$  lattice, as the inverse temperature is varied from  $\beta = 2$ – $14$ . We observe the formation of a plateau at  $\langle n \rangle = 2/3$  as the temperature is lowered, signaling the opening of a gap. No signatures of CDW ordering is observed at fillings away from  $\langle n \rangle = 2/3$  for these parameters. We also

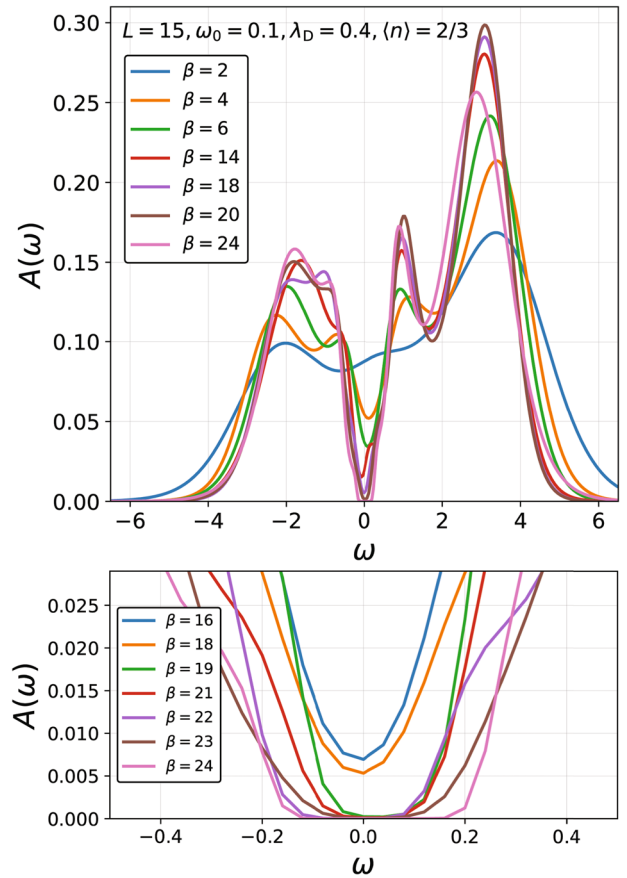


**Fig. 3 Spectral function.** Top: Momentum integrated spectral function  $A(\omega)$  shown for a range of inverse temperatures from  $\beta = 2$  to  $\beta = 24$ , at filling fraction  $\langle n \rangle = 2/3$  (with  $\omega_0 = 0.1$ ,  $\lambda_D = 0.4$ ). The linear lattice dimension is  $L = 15$  i.e.,  $N_s = 775$ . Bottom: a close-up view of the finite gap opening for  $\beta \gtrsim 18$  where  $A(\omega) = 0$ .

calculate the average electron kinetic energy as a function of electron density as shown in Fig. 2b. We observe a sharp change at  $\langle n \rangle = 2/3$ , where the magnitude of the electron kinetic energy becomes maximal. This is a signature of a CDW phase transition, since a configuration of doubly-occupied sites surrounded by empty nearest-neighbor sites maximizes the number of bonds along which electron hopping is permitted (and corresponds to an average electron density per site  $\langle n \rangle = 2/3$  on the kagome lattice). Note that since the kagome lattice is not bipartite, particle-hole symmetry is not present and thus both the kinetic energy and average filling are not symmetric about half-filling.

To further study the opening of a CDW gap as the temperature is lowered, we calculate the momentum integrated spectral function  $A(\omega)$ , which is related to the imaginary time dependent Green's function through the integral equation

$$G(\mathbf{k}, \tau) = \langle \hat{c}(\mathbf{k}, \tau) \hat{c}^\dagger(\mathbf{k}, \tau) \rangle = \int d\omega A(\mathbf{k}, \omega) \frac{e^{-\omega\tau}}{1 + e^{-\beta\omega}}, \quad (6)$$

which we invert using the maximum entropy method to obtain  $A(\omega)$ <sup>70</sup>. In Fig. 3, we show the momentum integrated spectral function for an  $L = 15$  lattice ( $N_s = 775$ ) for a range of temperatures down to  $\beta = 24$ , again fixing  $\omega_0 = 0.1$ ,  $\lambda_D = 0.4$ , and an average electron density per site of  $\langle n \rangle = 2/3$ . We observe three peaks in the spectral function corresponding to the three-band structure. As the temperature is lowered,  $A(\omega)$  reaches zero and a finite gap begins to open at  $\beta \gtrsim 18$ , as shown in the bottom panel, indicating a transition to an insulating CDW phase.

At an average electron density per site of  $\langle n \rangle = 2/3$ , the lower energy band is completely filled and touches the upper band at

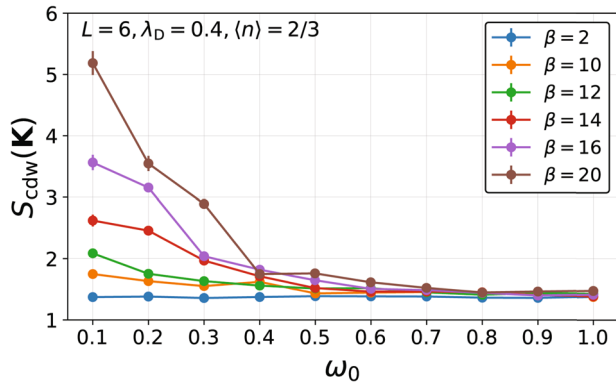


**Fig. 4 Charge structure factor vs. phonon frequency.** Charge structure factor  $S_{\text{cdw}}(\mathbf{K})$  as a function of phonon frequency, for a range of temperatures from  $\beta = 2$  to  $\beta = 20$ . Results are shown for an  $L = 6$  lattice at  $\langle n \rangle = 2/3, \lambda_D = 0.4$ . Error bars correspond to the standard deviation of the measured mean.

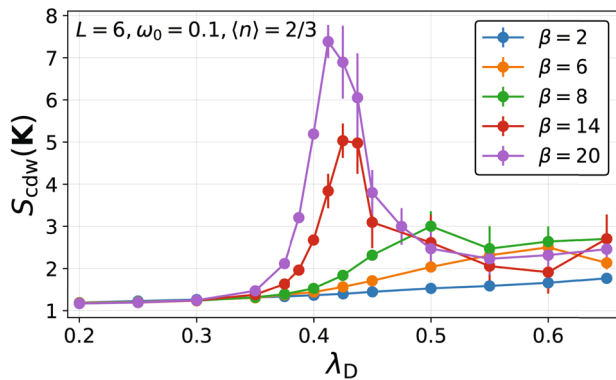


**Fig. 5 Charge structure factor vs.  $\lambda_D$ .** Charge structure factor  $S_{\text{cdw}}(\mathbf{K})$  as a function of the dimensionless electron-phonon coupling  $\lambda_D$ , for a range of temperatures from  $\beta = 2$  to  $\beta = 20$ . Results are shown for an  $L = 6$  lattice at  $\langle n \rangle = 2/3, \omega_0 = 0.1$ . Error bars correspond to the standard deviation of the measured mean.

the Dirac points  $K$  and  $K'$ . To study the onset of CDW order at this filling, we, therefore, calculate the charge structure factor  $S_{\text{cdw}}$  [Eq. (5)] evaluated at  $\mathbf{q} = \mathbf{K}$ , as a function of phonon frequency, electron-phonon coupling, and temperature.

In Fig. 4, we show the variation of  $S_{\text{cdw}}(\mathbf{K})$  as the phonon frequency  $\omega_0$  is increased from 0.1 to 1.0. In the antiadiabatic limit ( $\omega_0 \rightarrow \infty$ ), deformation of the lattice is weakened as sites respond more quickly to electron hopping and bipolarons do not readily localize, inhibiting the formation of a stable CDW pattern<sup>22</sup>. In addition, quantum fluctuations are enhanced at large  $\omega_0$ , further suppressing CDW order<sup>23</sup>. For  $\omega_0 \gtrsim 0.4$  we observe no significant growth in  $S_{\text{cdw}}(\mathbf{K})$  as the temperature is lowered from  $\beta = 2$  to  $\beta = 20$ . However, for  $\omega_0 \lesssim 0.3$ , the structure factor begins to increase in magnitude as the temperature is reduced, growing more rapidly with  $\beta$  as  $\omega_0 \rightarrow 0$ . We therefore fix  $\omega_0 = 0.1$ , and vary the dimensionless electron-phonon coupling  $\lambda_D$ , in order to determine the region in which CDW order at  $\langle n \rangle = 2/3$  is most enhanced and subsequently estimate  $T_c$  for these parameters.

At small values of  $\lambda_D$ , we find no enhancement in  $S_{\text{cdw}}(\mathbf{K})$  from  $\beta = 2$  to  $\beta = 20$  i.e., for  $\lambda_D \lesssim 0.3$  there is no sign of CDW order in this temperature range, as shown in Fig. 5. This may be due to the critical temperature becoming exponentially suppressed as  $\lambda_D \rightarrow 0$ . However, another possibility is a finite  $\lambda_D$  is necessary for CDW formation, as is the case in the honeycomb lattice Holstein model at half-filling<sup>25</sup>, which similarly has Dirac cones and a vanishing

density of states at the Fermi surface. As  $\lambda_D$  increases, the effective electron-electron attraction is enhanced, and we observe an increase in the charge structure factor as pairs of electrons arrange themselves into a periodic CDW. As the temperature is reduced, we find that there is a maximum in  $S_{\text{cdw}}(\mathbf{K})$  at approximately  $\lambda_D \approx 0.4$ . At larger  $\lambda_D$ , the CDW structure factor is smaller, and eventually no significant growth is observed as the temperature is lowered from  $\beta = 2$  to  $\beta = 20$ . This behavior might originate from the higher effective bipolaron mass at large  $\lambda_D$ , which will hinder their arrangement into an ordered CDW phase, as the energy barrier associated with moving from site to site is proportional to  $\lambda_D$ , thus promoting self-trapping. Consequently,  $T_c$  rapidly decreases as  $\lambda_D$  becomes much larger than its optimal value. We note that similar behavior has been observed in the honeycomb, square, and Lieb lattice Holstein models<sup>25,27</sup>.

The momentum dependence of  $S_{\text{cdw}}(\mathbf{q})$  is shown in Fig. 6, where the charge structure factor at  $\langle n \rangle = 2/3$  is evaluated over the first Brillouin zone for an  $L = 12$  lattice. An enhancement in the structure factor is observed at the Dirac points as the temperature is lowered, corresponding to the onset of an ordered CDW phase, with the magnitude of  $S_{\text{cdw}}$  increasing rapidly around  $\beta \gtrsim 17$ . For all other momentum values, including at the  $M$  and  $\Gamma$ -points, we find no enhancement in charge correlations with inverse temperature  $\beta$ , at this filling.

A real-space depiction of the CDW correlations at  $\langle n \rangle = 2/3$  is shown in Fig. 7, which plots density-density correlations  $\langle \hat{n}(\mathbf{r})\hat{n}(\mathbf{0}) \rangle$  over an  $L = 12$  lattice with periodic boundary conditions. Here  $\mathbf{r} = 0$  is the position of a fixed reference site belonging to the  $A$  sublattice. Hence Fig. 7 depicts  $c_{\alpha,\nu}(\mathbf{r})$  with the origin fixed at this reference site. The CDW pattern is characterized by the localization of electron pairs on only one site per unit cell, which belongs to either the  $A$ ,  $B$ , or  $C$  sublattice, alternating cyclically between these from one unit cell to the next (in both the  $\mathbf{a}_1$  and  $\mathbf{a}_2$  directions). The fact that  $\mathbf{K}$  and  $\mathbf{K}'$  are the ordering wavevectors for this pattern can be understood as follows. In terms of the reciprocal lattice vectors, we have  $\mathbf{K} = \frac{1}{3}(\mathbf{b}_1 - \mathbf{b}_2)$  and  $\mathbf{K}' = \frac{1}{3}(2\mathbf{b}_1 + \mathbf{b}_2)$ . If the doubly-occupied sites are separated by a displacement  $\mathbf{r} = n_1\mathbf{a}_1 + n_2\mathbf{a}_2$ , then the Fourier transform of the density-density correlation function will have peaks at  $\mathbf{K}$  or  $\mathbf{K}'$  if  $\mathbf{K} \cdot \mathbf{r} = 2m\pi$  or  $\mathbf{K}' \cdot \mathbf{r} = 2m\pi$ , where  $m \in \mathbb{Z}$ . This is satisfied if  $(n_1 - n_2) \bmod 3 = 0$  (for  $\mathbf{K}$ ) or  $(2n_1 + n_2) \bmod 3 = 0$  (for  $\mathbf{K}'$ ), which are equivalent conditions. In other words, moving along either the  $\mathbf{a}_1$  or  $\mathbf{a}_2$  directions, density-density correlations will repeat with a periodicity of three unit cells, i.e., for each unit cell, the site on which the electron pairs localize will alternate cyclically between the  $\{A, B, C\}$  sublattices. For any given unit cell, the onset of this type of CDW order therefore breaks a  $Z_3$  symmetry, and the phase transition should belong to the 3-state Potts model universality class.

### Estimation of $T_c$ for CDW phase

For an approximate estimate of the critical temperature we can examine when the correlations become long-ranged on a finite-size lattice. As shown in Fig. 7, at  $\beta = 16$  the charge order is emerging, but it is not quite long-ranged. At  $\beta = 20$  however, we see the periodic density correlations persist over the whole lattice. This suggests  $T_c$  should lie at an intermediate temperature between these two values; however, for a more accurate estimate, we must study the onset of charge order for several different lattice sizes.

In Fig. 8, we show the variation of the charge structure factor  $S_{\text{cdw}}(\mathbf{K})$  with inverse temperature  $\beta$ , for lattices with linear dimension  $L = 6, 9, 12$  and  $15$ , for a range of temperatures down to  $\beta = 24$ . At high temperatures,  $S_{\text{cdw}}(\mathbf{K})$  is relatively small and independent of lattice size. However, as the temperature is reduced,  $S_{\text{cdw}}(\mathbf{K})$  grows and becomes dependent on the lattice size for  $\beta \gtrsim 18$ . This signals that correlations are becoming long-

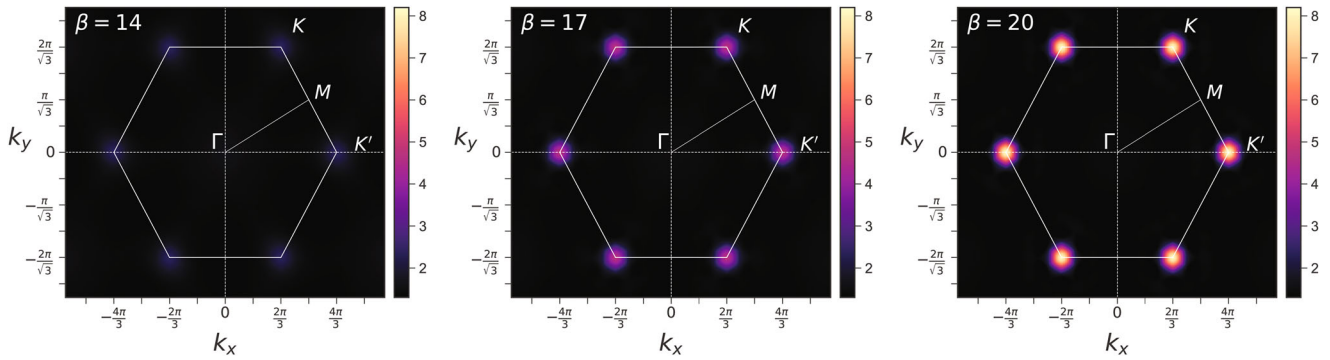


**Fig. 6 Charge structure factor in momentum space.** Charge structure factor  $S_{\text{cdw}}(\mathbf{q})$  shown across the Brillouin zone of the kagome lattice with  $L = 12$ , shown for  $\beta = 14, 17$  and  $20$ . The locations of high-symmetry points in momentum space at  $K = (2\pi/3, 2\pi/\sqrt{3})$ ,  $K' = (4\pi/3, 0)$ ,  $M = (\pi, \pi/\sqrt{3})$ , and  $\Gamma = (0, 0)$  are indicated.

ranged and thus sensitive to system size on a finite lattice, and suggests a critical temperature of  $\beta_c \approx 18$ . A more accurate determination of  $T_c$  can be made by studying the correlation ratio

$$R_c = 1 - \frac{S_{\text{cdw}}(\mathbf{q} + \mathbf{d}\mathbf{q})}{S_{\text{cdw}}(\mathbf{q})}, \quad (7)$$

where the ordering wavevector  $\mathbf{q} = \mathbf{K}$  here, and  $|\mathbf{d}\mathbf{q}|$  is the spacing between discrete momentum values for a lattice of linear dimension  $L$ . For the kagome lattice we average over the six nearest neighbors of the  $K$ -point in momentum space to obtain  $S(\mathbf{K} + \mathbf{d}\mathbf{q})$ . The correlation ratio  $R_c$  is defined such that in the CDW phase,  $R_c \rightarrow 1$  as  $L \rightarrow \infty$ , (since  $S_{\text{cdw}}(\mathbf{q})$  will diverge with  $L$  if there is long-range order), while  $R_c \rightarrow 0$  if there is no long-range order. When plotted for different lattice sizes, the crossing of  $R_c$  curves gives an estimate of the critical point. In Fig. 9, we plot  $R_c$  for lattices with  $L = 6, 9, 12$ , and  $15$ , for the same parameters as in Fig. 8 ( $\langle n \rangle = 2/3$ ,  $\omega_0 = 0.1$ ,  $\lambda_D = 0.4$ ). There is a crossing at  $\beta_c \approx 18$ , which is consistent with our previous estimates of  $\beta_c$  obtained from observing the opening of a finite gap in  $A(\omega)$ , the onset of long-ranged density-density correlations, and the temperature at which  $S_{\text{cdw}}$  becomes dependent on lattice size.

Thus far, we have studied the emergence of CDW order on the kagome lattice at a fixed electron density of  $\langle n \rangle = 2/3$  per site. This choice was motivated by the observation of a CDW gap at  $\langle n \rangle = 2/3$  and a sharp change in electron kinetic energy during sweeps of  $\mu$  and  $\langle n \rangle$ , and the fact that this filling corresponds to a completely filled lower band, which meets the middle band at the Dirac points  $K$  and  $K'$ . However, we also considered fillings of  $\langle n \rangle = 1/2$  and  $\langle n \rangle = 5/6$ , i.e., densities at which the saddle points in the non-interacting band structure (at the  $M$ -points) and their van Hove singularities are at the Fermi energy. We also consider  $\langle n \rangle = 4/3$ , which corresponds to completely filled lower and middle bands, with a quadratic touching at the  $\Gamma$ -point between the flat and middle bands (see Fig. 1). In all of these cases, we find no evidence for the formation of a CDW. For example, there are no anomalous features in components of the total energy, or any indications of a plateau in the  $\langle n \rangle$  vs.  $\mu$  plots near these fillings, as shown in Fig. 2. Moreover, as the temperature is lowered ( $\beta$  increases) the charge structure factor  $S_{\text{cdw}}(\mathbf{q})$  does not grow significantly and remains relatively small in magnitude, as shown in Fig. 10 for several high-symmetry points  $\mathbf{q}$  in the Brillouin zone [ $\Gamma = (0, 0)$ ,  $\mathbf{K} = (\frac{2\pi}{3}, \frac{2\pi}{\sqrt{3}})$ , and  $\mathbf{M} = (\pi, \frac{\pi}{\sqrt{3}})$ ]. We fix  $\omega_0 = 0.1$  here to avoid suppression of any potential CDW order, which occurs in the antiadiabatic limit. These results thus suggest an absence of any charge ordering at these fillings, at least for inverse temperatures  $\beta < 20$ . In other words, our results show no evidence for other varieties of CDW order in the kagome lattice Holstein model other than at the  $K$ -points at  $\langle n \rangle = 2/3$ .

## DISCUSSION

We performed hybrid Monte Carlo simulations of the Holstein model on the kagome lattice on systems of up to  $N_s = 775$  sites, and studied the onset of CDW order while varying the electron filling, phonon frequency, electron-phonon coupling, and temperature. Our HMC algorithm allows us to simulate larger system sizes and access lower, more realistic phonon frequencies than in previous DMQC studies of the Holstein model. We observe evidence of CDW order at an average electron density of  $\langle n \rangle = 2/3$  per site (i.e., an overall filling fraction of  $f = 1/3$ ), signaled by the opening of a gap in  $A(\omega)$  at the Fermi surface, long-ranged density-density correlations, and the extensive scaling of the charge structure factor  $S_{\text{cdw}}(\mathbf{K})$  below the critical temperature. From our analysis of the correlation ratio  $R_c$ , we estimate a CDW transition at  $T_c \approx t/18 = W/108$ , where  $W$  is the non-interacting electronic bandwidth.

This value of  $T_c$  is notably lower than the CDW transition temperatures found in the Holstein model on alternative geometries, e.g., at  $\lambda_D = 0.4$ ,  $T_c \approx t/6$  on the honeycomb and Lieb lattices, while  $T_c \approx t/4$  on the square lattice<sup>25,27</sup>. Moreover, the CDW order appears only for a narrow range of electron-phonon coupling strengths in the kagome lattice, peaked at  $\lambda_D \approx 0.4$  (for  $\omega_0/t = 0.1$ ). In contrast, previous Holstein model studies on square, honeycomb, and Lieb lattices have found CDW transitions across a broad range  $\lambda_D \in [0.25, 1]$ <sup>22,25,27</sup>. On bipartite geometries with equal numbers of  $A$  and  $B$  sites, such as the square and honeycomb lattices, CDW formation in the Holstein model occurs at half-filling i.e.,  $\langle n \rangle = 1$ . However, on the Lieb lattice, for which  $N_A \neq N_B$ , when CDW order forms the density shifts away from half-filled to either  $\langle n \rangle = 2/3$  or  $\langle n \rangle = 4/3$ , corresponding to completely filled lower and flat bands, respectively<sup>27</sup>. Although the kagome lattice similarly exhibits a three-band structure, the geometry is frustrated, unlike the Lieb case, and we find that charge order emerges only at  $\langle n \rangle = 2/3$  for temperatures  $T \geq t/20$  with an ordering wavevector at the  $K$ -points and a  $\sqrt{3} \times \sqrt{3}$  supercell. Our simulations did not reveal CDW order at other ordering momenta or electron densities, including at the van Hove filling.

The CDW order we find is analogous to the  $\sqrt{3} \times \sqrt{3}$  long-range magnetic order observed in the kagome lattice Heisenberg antiferromagnet, when it is coupled to local site-phonon modes<sup>32</sup>. The same CDW phase has also been proposed as the ground state in certain regimes of the extended Hubbard model<sup>40,41</sup>, i.e., at fillings of  $\langle n \rangle = 2/3$  and  $\langle n \rangle = 5/6$  for large  $V/U$ , where  $U$  is the on-site Hubbard term and  $V$  is the nearest-neighbor repulsion, and has been termed CDW-III in these studies.

It should be noted that the CDW order we observe does not correspond to the star-of-David or inverse star-of-David patterns observed recently in kagome metals such as  $\text{AV}_3\text{Sb}_5$  ( $A = \text{K, Rb, Cs}$ ), which exhibit ordering at the  $M$ -points. A recent work<sup>41</sup> showed that such a CDW ordering is observed in the kagome

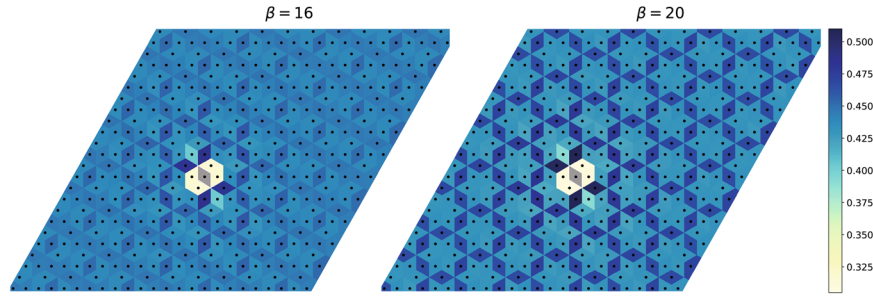


**Fig. 7 Real space density-density correlations.** Real space density-density correlations  $\langle \hat{n}(\mathbf{0})\hat{n}(\mathbf{r}) \rangle$ , where  $\hat{n}(\mathbf{0})$  denotes the electron density at a reference site located at the origin (gray region). For each site at position  $\mathbf{r}$ , the color of its Voronoi cell indicates the magnitude of  $\langle \hat{n}(\mathbf{0})\hat{n}(\mathbf{r}) \rangle$ . Results are shown for an  $L = 12$  lattice with periodic boundary conditions, for  $\beta = 16$  (left) and  $\beta = 20$  (right) at filling  $\langle n \rangle = 2/3$  (with  $\lambda_D = 0.4$  and  $\omega = 0.1$ ).

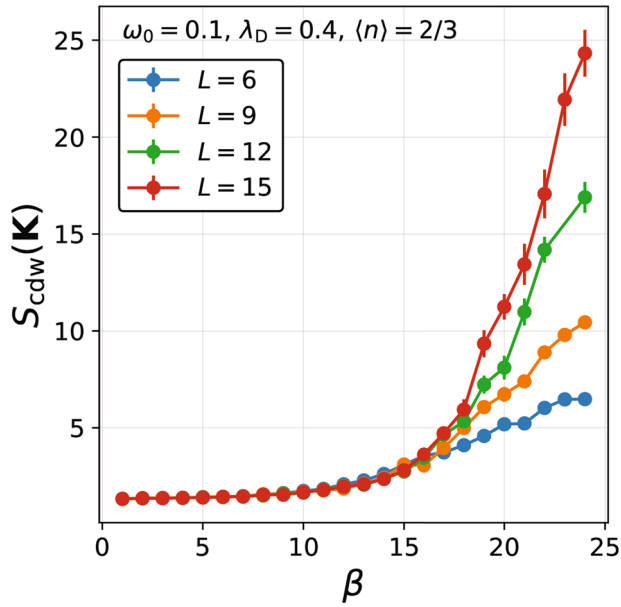


**Fig. 8 Charge structure factor vs. inverse temperature.** Charge structure factor  $S_{\text{cdw}}(\mathbf{K})$  as a function of inverse temperature  $\beta$ , for lattice sizes  $L = 6, 9, 12$  and  $15$ , at filling  $\langle n \rangle = 2/3$ . A lattice size dependence in the order parameter emerges at  $\beta \gtrsim 18$ , indicating the onset of CDW order. Here, we fix  $\lambda_D = 0.4$  and  $\omega_0 = 0.1$ . Error bars correspond to the standard deviation of the measured mean.

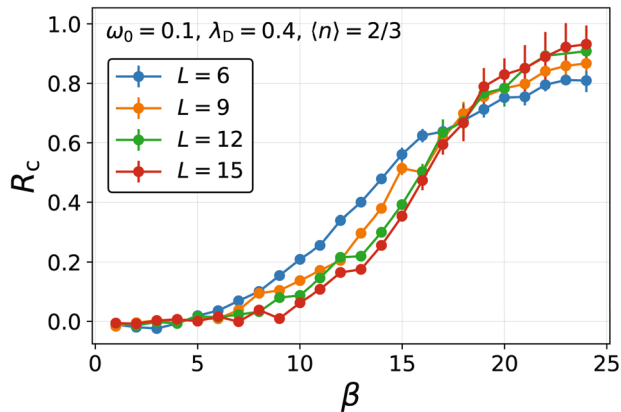


**Fig. 9 Correlation ratio crossing.** Correlation ratio  $R_c$  as a function of  $\beta$ , showing a crossing at  $\beta_c \approx 18$ . Data is shown for lattice sizes  $L = 6, 9, 12$  and  $15$ , for the same parameters as in Fig. 8.

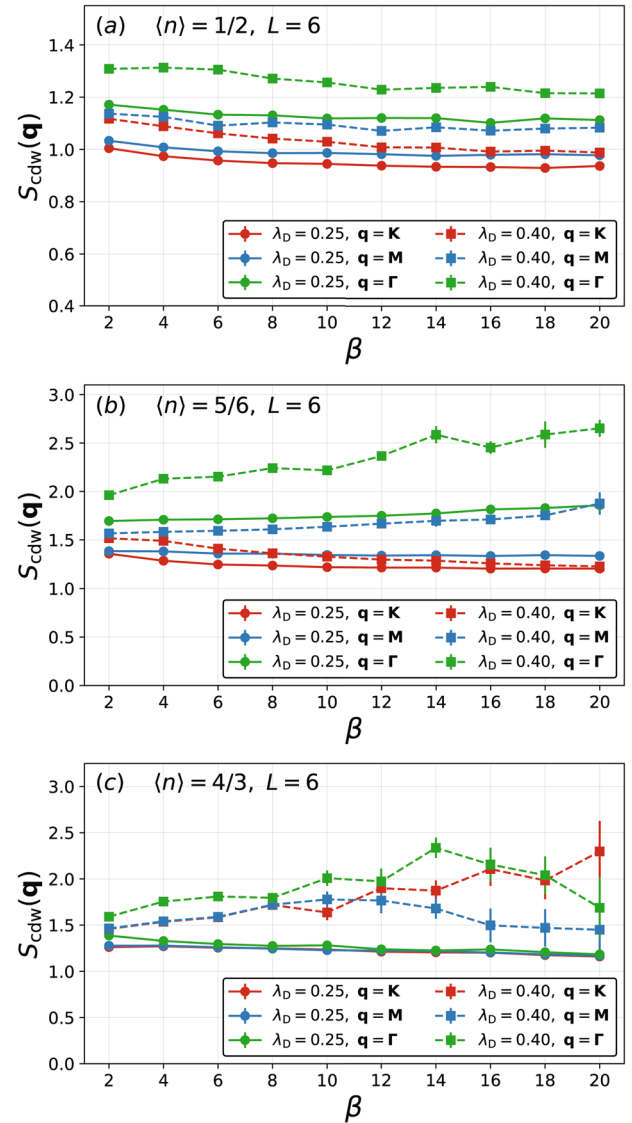


**Fig. 10  $S_{\text{cdw}}(\mathbf{q})$  at  $\langle n \rangle = 1/2, 5/6$ , and  $4/3$ .** Charge structure factor  $S_{\text{cdw}}(\mathbf{q})$  as a function of inverse temperature  $\beta$  at several fixed electron densities: (a)  $\langle n \rangle = 1/2$ , (b)  $\langle n \rangle = 5/6$ , and (c)  $\langle n \rangle = 4/3$ , for an  $L = 6$  lattice. Data is shown for  $\lambda_D = 0.25$  (solid line) and  $\lambda_D = 0.40$  (dashed line) for several momenta  $\mathbf{q}$ :  $\Gamma = (0, 0)$ ,  $\mathbf{K} = (\frac{2\pi}{3}, \frac{2\pi}{3})$ , and  $\mathbf{M} = (\pi, \frac{\pi}{3})$ . The phonon frequency is fixed at  $\omega_0 = 0.1$ . Error bars correspond to the standard deviation of the measured mean.

lattice Hubbard model when a Su–Schrieffer–Heeger electron-phonon coupling is introduced. Here, the electron-phonon coupling modulates the electron hopping term, and is conceptually distinct from Holstein model, in which electrons and phonons interact on a single site, rather than on the bonds of the lattice.

## METHODS

### Hybrid Monte Carlo simulation

Previous finite temperature studies of the Holstein model have typically employed DQMC<sup>71,72</sup>. In this method, the inverse temperature  $\beta = L_t \Delta\tau$  is discretized along an imaginary time axis with  $L_t$  intervals of length  $\Delta\tau$ , and the partition function is expressed as  $Z = \text{Tr} e^{-\beta\hat{H}} = \text{Tr} e^{-\Delta\tau\hat{H}} e^{-\Delta\tau\hat{H}} \dots e^{-\Delta\tau\hat{H}}$ . Since Eq. (1) is quadratic in fermionic operators, these can be traced out, giving an expression for  $Z$  in terms of the product of two identical matrix determinants  $\det M(x_{i,\tau})$ , which are functions of the space and time-dependent phonon displacement field only. Monte Carlo sampling using local updates to the phonon field  $\{x_{i,\tau}\}$  is performed and physical quantities can be measured through the fermion Green's function  $G_{ij} = \langle c_i^\dagger c_j \rangle = [M^{-1}]_{ij}$ . Although there is no sign problem<sup>73</sup> for the Holstein model, these studies have been limited for two main reasons. First, the computational cost of DQMC scales as  $N_s^3 L_t$ , where  $N_s$  is the total number of lattice sites, prohibiting the study of large system sizes. Secondly, the restriction to local updates results in long autocorrelation times at small phonon frequencies. This aspect has limited simulations to phonon frequencies of  $\omega_0 \gtrsim t$ , which is unrealistic for most real materials, and is far from the regime where CDW order in the Holstein model is typically the strongest ( $\omega_0 \ll t$ ).

Significant efficiency gains are possible by using a dynamical sampling procedure that updates the entire phonon field at each time-step<sup>74,75</sup>. In this work, we use a recently developed collection of techniques to perform finite temperature simulations on extremely large clusters<sup>68</sup>. Our HMC-based approach achieves a near-linear scaling with system size<sup>74,76,77</sup>, allowing us to study lattices of up to  $N_s = 775$  sites at temperatures as low as  $T = t/24$ . Our algorithm efficiently updates the phonon field simultaneously, allowing study of a realistic phonon frequency  $\omega_0/t = 0.1$ .

Near-linear scaling is achieved by rewriting each matrix determinant  $\det M$  as a multi-dimensional Gaussian integral involving auxiliary fields  $\Phi_\sigma$  that will also be sampled. Here, the partition function becomes

$$\mathcal{Z} \approx (2\pi)^{N_s L_t} \int \mathcal{D}\Phi_\uparrow \mathcal{D}\Phi_\downarrow \mathcal{D}x e^{-S(x, \Phi_\sigma)}, \quad (8)$$

where the total action is

$$S(x, \Phi_\sigma) = S_B(x) + S_F(x, \Phi_\sigma) \quad (9)$$

with the fermionic (F) and bosonic (B) contributions

$$S_F(x, \Phi_\sigma) = \frac{1}{2} \sum_\sigma \Phi_\sigma^T (M^T M)^{-1} \Phi_\sigma \quad (10)$$

$$S_B(x) = \frac{\Delta\tau}{2} \sum_{i,\tau} \left[ \omega_0^2 x_{i,\tau}^2 + \left( \frac{x_{i,\tau+1} - x_{i,\tau}}{\Delta\tau} \right)^2 \right]. \quad (11)$$

A Gibbs sampling procedure is then adopted where  $\Phi_\sigma$  and  $x$  are alternately updated. The auxiliary field  $\Phi_\sigma$  may be directly sampled. Using HMC, global updates to the phonon fields  $x$  can be performed by introducing a conjugate momentum  $p$  and evolving a fictitious Hamiltonian dynamics using a symplectic integrator<sup>68</sup>.

## DATA AVAILABILITY

The data that support the findings of this study will be made available upon reasonable requests to the corresponding author.

## CODE AVAILABILITY

The HMC code used in this study is available at <https://github.com/cohensbw/EIPhDynamics>.

Received: 7 January 2023; Accepted: 14 April 2023;

Published online: 06 May 2023

## REFERENCES

- Grüner, G. The dynamics of charge-density waves. *Rev. Mod. Phys.* **60**, 1129–1181 (1988).
- Gor'kov, L. & Grüner, G. *Charge Density Waves in Solids*, vol. 25 of *Modern Problems in Condensed Matter Physics* (North Holland, 1989).
- Zhu, X., Cao, Y., Zhang, J., Plummer, E. W. & Guo, J. Classification of charge density waves based on their nature. *Proc. Natl Acad. Sci. USA* **112**, 2367–2371 (2015).
- Migdal, A. Interactions between electrons and lattice vibrations in a normal metal. *J. Exp. Theor. Phys.* **34**, 1438–1446 (1958).
- Eliashberg, G. Interactions between electrons and lattice vibrations in a superconductor. *J. Exp. Theor. Phys.* **38**, 966–976 (1960).
- Bardeen, J., Cooper, L. N. & Schrieffer, J. R. Theory of superconductivity. *Phys. Rev.* **108**, 1175–1204 (1957).
- Holstein, T. Studies of polaron motion: part I. The molecular-crystal model. *Ann. Phys.* **8**, 325–342 (1959).
- Scalettar, R. T., Bickers, N. E. & Scalapino, D. J. Competition of pairing and Peierls-charge-density-wave correlations in a two-dimensional electron-phonon model. *Phys. Rev. B* **40**, 197–200 (1989).
- Noack, R. M., Scalapino, D. J. & Scalettar, R. T. Charge-density-wave and pairing susceptibilities in a two-dimensional electron-phonon model. *Phys. Rev. Lett.* **66**, 778–781 (1991).
- Vekić, M., Noack, R. M. & White, S. R. Charge-density waves versus superconductivity in the Holstein model with next-nearest-neighbor hopping. *Phys. Rev. B* **46**, 271–278 (1992).
- Niyaz, P., Gubernatis, J. E., Scalettar, R. T. & Fong, C. Y. Charge-density-wave-gap formation in the two-dimensional Holstein model at half-filling. *Phys. Rev. B* **48**, 16011–16022 (1993).
- Marsiglio, F. Pairing and charge-density-wave correlations in the Holstein model at half-filling. *Phys. Rev. B* **42**, 2416–2424 (1990).
- Costa, N. C., Blommel, T., Chiu, W.-T., Batrouni, G. & Scalettar, R. T. Phonon dispersion and the competition between pairing and charge order. *Phys. Rev. Lett.* **120**, 187003 (2018).
- Cohen-Stead, B., Costa, N. C., Khatami, E. & Scalettar, R. T. Effect of strain on charge density wave order in the Holstein model. *Phys. Rev. B* **100**, 045125 (2019).
- Xiao, B., Costa, N. C., Khatami, E., Batrouni, G. G. & Scalettar, R. T. Charge density wave and superconductivity in the disordered Holstein model. *Phys. Rev. B* **103**, L060501 (2021).
- Hohenadler, M. & Batrouni, G. G. Dominant charge density wave correlations in the Holstein model on the half-filled square lattice. *Phys. Rev. B* **100**, 165114 (2019).
- Johnston, S. et al. Determinant quantum Monte Carlo study of the two-dimensional single-band Hubbard-Holstein model. *Phys. Rev. B* **87**, 235133 (2013).
- Bradley, O., Batrouni, G. G. & Scalettar, R. T. Superconductivity and charge density wave order in the two-dimensional Holstein model. *Phys. Rev. B* **103**, 235104 (2021).
- Esterlis, I. et al. Breakdown of the Migdal-Eliashberg theory: a determinant quantum Monte Carlo study. *Phys. Rev. B* **97**, 140501 (2018).
- Dee, P. M., Nakatsukasa, K., Wang, Y. & Johnston, S. Temperature-filling phase diagram of the two-dimensional Holstein model in the thermodynamic limit by self-consistent Migdal approximation. *Phys. Rev. B* **99**, 024514 (2019).
- Dee, P. M., Coulter, J., Kleiner, K. G. & Johnston, S. Relative importance of non-linear electron-phonon coupling and vertex corrections in the Holstein model. *Commun. Phys.* **3**, 145 (2020).
- Nosarzewski, B. et al. Superconductivity, charge density waves, and bipolarons in the Holstein model. *Phys. Rev. B* **103**, 235156 (2021).
- Li, Z.-X., Cohen, M. L. & Lee, D.-H. Enhancement of superconductivity by frustrating the charge order. *Phys. Rev. B* **100**, 245105 (2019).
- Cohen-Stead, B. et al. Langevin simulations of the half-filled cubic Holstein model. *Phys. Rev. B* **102**, 161108 (2020).
- Zhang, Y.-X., Chiu, W.-T., Costa, N. C., Batrouni, G. G. & Scalettar, R. T. Charge order in the Holstein model on a honeycomb lattice. *Phys. Rev. Lett.* **122**, 077602 (2019).
- Feng, C., Guo, H. & Scalettar, R. T. Charge density waves on a half-filled decorated honeycomb lattice. *Phys. Rev. B* **101**, 205103 (2020).
- Feng, C. & Scalettar, R. T. Interplay of flat electronic bands with Holstein phonons. *Phys. Rev. B* **102**, 235152 (2020).

28. Singh, R. R. P. & Huse, D. A. Ground state of the spin-1/2 kagome-lattice Heisenberg antiferromagnet. *Phys. Rev. B* **76**, 180407 (2007).
29. Yan, S., Huse, D. A. & White, S. R. Spin-Liquid ground state of the  $S = 1/2$  kagome Heisenberg antiferromagnet. *Science* **332**, 1173–1176 (2011).
30. Liao, H. J. et al. Gapless spin-liquid ground state in the  $S = 1/2$  kagome antiferromagnet. *Phys. Rev. Lett.* **118**, 137202 (2017).
31. Läuchli, A. M., Sudan, J. & Moessner, R.  $S = \frac{1}{2}$  kagome Heisenberg antiferromagnet revisited. *Phys. Rev. B* **100**, 155142 (2019).
32. Gen, M. & Suwa, H. Nematicity and fractional magnetization plateaus induced by spin-lattice coupling in the classical kagome-lattice Heisenberg antiferromagnet. *Phys. Rev. B* **105**, 174424 (2022).
33. Ohashi, T., Kawakami, N. & Tsunetsugu, H. Mott transition in kagomé lattice Hubbard model. *Phys. Rev. Lett.* **97**, 066401 (2006).
34. Ohashi, T., Suga, S.-I., Kawakami, N. & Tsunetsugu, H. Magnetic correlations around the Mott transition in the kagomé lattice Hubbard model. *J. Phys. Cond. Mat.* **19**, 145251 (2007).
35. Kaufmann, J., Steiner, K., Scalettar, R. T., Held, K. & Janson, O. How correlations change the magnetic structure factor of the kagome Hubbard model. *Phys. Rev. B* **104**, 165127 (2021).
36. Higa, R. & Asano, K. Bond formation effects on the metal-insulator transition in the half-filled kagome Hubbard model. *Phys. Rev. B* **93**, 245123 (2016).
37. Sun, R.-Y. & Zhu, Z. Metal-insulator transition and intermediate phases in the kagome lattice Hubbard model. *Phys. Rev. B* **104**, L121118 (2021).
38. Kiesel, M. L., Platt, C. & Thomale, R. Unconventional Fermi surface instabilities in the kagome Hubbard model. *Phys. Rev. Lett.* **110**, 126405 (2013).
39. Wang, W.-S., Li, Z.-Z., Xiang, Y.-Y. & Wang, Q.-H. Competing electronic orders on kagome lattices at van Hove filling. *Phys. Rev. B* **87**, 115135 (2013).
40. Wen, J., Rüegg, A., Wang, C.-C. J. & Fiete, G. A. Interaction-driven topological insulators on the kagome and the decorated honeycomb lattices. *Phys. Rev. B* **82**, 075125 (2010).
41. Ferrari, F., Becca, F. & Valentí, R. Charge density waves in kagome-lattice extended Hubbard models at the van Hove filling. *Phys. Rev. B* **106**, L081107 (2022).
42. Zhu, X., Han, W., Feng, S. & Guo, H. Quantum Monte Carlo study of the attractive kagome-lattice Hubbard model. *Phys. Rev. Res.* **5**, 023037 (2023).
43. Nguyen, T. & Li, M. Electronic properties of correlated kagomé metals  $AV_3Sb_5$  ( $A = K, Rb$ , and  $Cs$ ): a perspective. *J. Appl. Phys.* **131**, 060901 (2022).
44. Ortiz, B. R. et al. New kagome prototype materials: discovery of  $KV_3Sb_5$ ,  $RbV_3Sb_5$ , and  $CsV_3Sb_5$ . *Phys. Rev. Mater.* **3**, 094407 (2019).
45. Jiang, Y.-X. et al. Unconventional chiral charge order in kagome superconductor  $KV_3Sb_5$ . *Nat. Mater.* **20**, 1353–1357 (2021).
46. Zhao, H. et al. Cascade of correlated electron states in the kagome superconductor  $CsV_3Sb_5$ . *Nature* **599**, 216–221 (2021).
47. Ortiz, B. R. et al. Fermi surface mapping and the nature of charge-density-wave order in the kagome superconductor  $CsV_3Sb_5$ . *Phys. Rev. X* **11**, 041030 (2021).
48. Li, H. et al. Observation of unconventional charge density wave without acoustic phonon anomaly in kagome superconductors  $AV_3Sb_5$  ( $A = Rb, Cs$ ). *Phys. Rev. X* **11**, 031050 (2021).
49. Zhou, X. et al. Origin of charge density wave in the kagome metal  $CsV_3Sb_5$  as revealed by optical spectroscopy. *Phys. Rev. B* **104**, L041101 (2021).
50. Ratcliff, N., Hallett, L., Ortiz, B. R., Wilson, S. D. & Harter, J. W. Coherent phonon spectroscopy and interlayer modulation of charge density wave order in the kagome metal  $CsV_3Sb_5$ . *Phys. Rev. Mater.* **5**, L111801 (2021).
51. Kang, M. et al. Twofold van Hove singularity and origin of charge order in topological kagome superconductor  $CsV_3Sb_5$ . *Nat. Phys.* **18**, 301–308 (2022).
52. Xie, Y. et al. Electron-phonon coupling in the charge density wave state of  $CsV_3Sb_5$ . *Phys. Rev. B* **105**, L140501 (2022).
53. Wu, S. et al. Charge density wave order in the kagome metal  $AV_3Sb_5$  ( $A = Cs, Rb, K$ ). *Phys. Rev. B* **105**, 155106 (2022).
54. Kang, M. et al. Topological flat bands in frustrated kagome lattice  $CoSn$ . *Nat. Commun.* **11**, 4004 (2020).
55. Yin, J.-X. et al. Fermion-boson many-body interplay in a frustrated kagome paramagnet. *Nat. Commun.* **11**, 4003 (2020).
56. Park, T., Ye, M. & Balents, L. Electronic instabilities of kagome metals: saddle points and Landau theory. *Phys. Rev. B* **104**, 035142 (2021).
57. Ye, Z., Luo, A., Yin, J.-X., Hasan, M. Z. & Xu, G. Structural instability and charge modulations in the kagome superconductor  $AV_3Sb_5$ . *Phys. Rev. B* **105**, 245121 (2022).
58. Wang, C., Liu, S., Jeon, H. & Cho, J.-H. Origin of charge density wave in the layered kagome metal  $CsV_3Sb_5$ . *Phys. Rev. B* **105**, 045135 (2022).
59. Denner, M. M., Thomale, R. & Neupert, T. Analysis of charge order in the kagome metal  $AV_3Sb_5$  ( $A = K, Rb, Cs$ ). *Phys. Rev. Lett.* **127**, 217601 (2021).
60. Tan, H., Liu, Y., Wang, Z. & Yan, B. Charge density waves and electronic properties of superconducting kagome metals. *Phys. Rev. Lett.* **127**, 046401 (2021).
61. Christensen, M. H., Biroli, T., Andersen, B. M. & Fernandes, R. M. Theory of the charge density wave in  $AV_3Sb_5$  kagome metals. *Phys. Rev. B* **104**, 214513 (2021).
62. Lin, Y.-P. & Nandkishore, R. M. Complex charge density waves at Van Hove singularity on hexagonal lattices: Haldane-model phase diagram and potential realization in the kagome metals  $AV_3Sb_5$  ( $A = K, Rb, Cs$ ). *Phys. Rev. B* **104**, 045122 (2021).
63. Feng, X., Jiang, K., Wang, Z. & Hu, J. Chiral flux phase in the kagome superconductor  $AV_3Sb_5$ . *Sci. Bull.* **66**, 1384–1388 (2021).
64. Feng, X., Zhang, Y., Jiang, K. & Hu, J. Low-energy effective theory and symmetry classification of flux phases on the kagome lattice. *Phys. Rev. B* **104**, 165136 (2021).
65. Ruostekoski, J. Optical kagome lattice for ultracold atoms with nearest neighbor interactions. *Phys. Rev. Lett.* **103**, 080406 (2009).
66. Jo, G.-B. et al. Ultracold atoms in a tunable optical kagome lattice. *Phys. Rev. Lett.* **108**, 045305 (2012).
67. Samajdar, R., Ho, W. W., Pichler, H., Lukin, M. D. & Sachdev, S. Quantum phases of Rydberg atoms on a kagome lattice. *Proc. Natl Acad. Sci. USA* **118**, e2015785118 (2021).
68. Cohen-Stead, B. et al. Fast and scalable quantum Monte Carlo simulations of electron-phonon models. *Phys. Rev. E* **105**, 065302 (2022).
69. Miles, C. et al. Dynamical tuning of the chemical potential to achieve a target particle number in grand canonical Monte Carlo simulations. *Phys. Rev. E* **105**, 045311 (2022).
70. Kaufmann, J. & Held, K. ana\_cont: Python package for analytic continuation. *Comput. Phys. Commun.* **282**, 108519 (2023).
71. Blankenbecler, R., Scalapino, D. J. & Sugar, R. L. Monte Carlo calculations of coupled boson-fermion systems. I. *Phys. Rev. D* **24**, 2278–2286 (1981).
72. White, S. R. et al. Numerical study of the two-dimensional Hubbard model. *Phys. Rev. B* **40**, 506–516 (1989).
73. Loh, E. Y. et al. Sign problem in the numerical simulation of many-electron systems. *Phys. Rev. B* **41**, 9301–9307 (1990).
74. Beyl, S., Goth, F. & Assaad, F. F. Revisiting the hybrid quantum Monte Carlo method for Hubbard and electron-phonon models. *Phys. Rev. B* **97**, 085144 (2018).
75. Batrouni, G. G. & Scalettar, R. T. Langevin simulations of a long-range electron-phonon model. *Phys. Rev. B* **99**, 035114 (2019).
76. Duane, S., Kennedy, A., Pendleton, B. J. & Roweth, D. Hybrid Monte Carlo. *Phys. Lett. B* **195**, 216–222 (1987).
77. Cohen-Stead, B., Barros, K., Scalettar, R. & Johnston, S. A hybrid Monte Carlo study of bond-stretching electron-phonon interactions and charge order in  $BaBiO_3$ . *NPJ Comput. Mater.* **9**, 40 (2023).

## ACKNOWLEDGEMENTS

The work of O.B., B.C.-S., S.J., and R.T.S. were supported by the U.S. Department of Energy, Office of Science, Office of Basic Energy Sciences, under Award Number DE-SC0022311. K.B. acknowledges support from the Center of Materials Theory as a part of the Computational Materials Science (CMS) program, funded by the U.S. Department of Energy, Office of Basic Energy Sciences.

## AUTHOR CONTRIBUTIONS

O.B. performed the simulations and carried out the calculations. B.C.-S. and K.B. developed the computer codes. R.T.S. supervised the project. All authors discussed and analysed the results, and contributed to writing the paper.

## COMPETING INTERESTS

The authors declare no competing interests.

## ADDITIONAL INFORMATION

**Supplementary information** The online version contains supplementary material available at <https://doi.org/10.1038/s41535-023-00553-y>.

**Correspondence** and requests for materials should be addressed to Owen Bradley.

**Reprints and permission information** is available at <http://www.nature.com/reprints>

**Publisher's note** Springer Nature remains neutral with regard to jurisdictional claims in published maps and institutional affiliations.



**Open Access** This article is licensed under a Creative Commons Attribution 4.0 International License, which permits use, sharing, adaptation, distribution and reproduction in any medium or format, as long as you give appropriate credit to the original author(s) and the source, provide a link to the Creative Commons license, and indicate if changes were made. The images or other third party material in this article are included in the article's Creative Commons license, unless indicated otherwise in a credit line to the material. If material is not included in the article's Creative Commons license and your intended use is not permitted by statutory regulation or exceeds the permitted use, you will need to obtain permission directly from the copyright holder. To view a copy of this license, visit <http://creativecommons.org/licenses/by/4.0/>.

© The Author(s) 2023